INTERNATIONAL JOURNAL OF HYDROGEN ENERGY 46 (2021) 27801–27815

Available online at www.sciencedirect.com

ScienceDirect

journal homepage: www.elsevier.com/locate/he

Optical diagnostics in a detonation-driven direct-connected circular combustor fueled with hydrogen for mach 10 scramjet

GongXi Zhou [a,b], Xu Zhang [a], Jinping Li [a], Xiaoyuan Zhang [a], Shizhong Zhang [a], Xin Lin [a], Fei Li [a,*], Hong Chen [a], Lianjie Yue [a,b], XiLong Yu [a,b]

[a] State Key Laboratory of High Temperature Gas Dynamics, Institute of Mechanics, CAS, Beijing, 100190, China
[b] School of Engineering Science, University of Chinese Academy of Sciences, Beijing, 100049, China

HIGHLIGHTS

- Optical diagnosis of scramjet combustor with circular cross section and high Mach number were carried out.
- The different flame structures produced by different injection methods were studied by multi-view synchronous imaging.
- TDLAS is used to determine the effective working time of the direct-connected hydrogen-oxygen detonation driven test platform.
- The pulsation frequency of high Mach number flame is investigated by POD analysis.

ARTICLE INFO

Article history:
Received 10 February 2021
Received in revised form
31 May 2021
Accepted 1 June 2021
Available online 21 June 2021

Keywords:
High mach number scramjet
Circular cross-section
TDLAS
Multi-view simultaneous imaging
POD

ABSTRACT

Various optical methods are applied to study flame characteristics of a circular-cross-section combustor for a Mach 10 scramjet. Experiments are performed on a direct-connected test facility fueled by hydrogen and driven using hydrogen/oxygen detonation. The circular-cross-section combustor is advantageous in solving thermal inhomogeneity, corner boundary layer and aircraft integration problems. However, it is difficult to use traditional optical measurement methods, which require large-sized measurement windows. In this study, tunable diode laser spectroscopy and a multi-view imaging system are used with small windows. High repetition rate measurements allow the effective time of facility, which is approximately 5 ms in this case, to be obtained. The dynamic flame characteristics are diagnosed upstream and downstream of the cavity with/without strut injection. When combined with proper orthogonal decomposition to obtain the flame pulsation state during the effective time period, the method is expected to be effective for engine performance evaluation and numerical simulation verification.

* *Corresponding author.*
E-mail address: lifei@imech.ac.cn (F. Li).

https://doi.org/10.1016/j.ijhydene.2021.06.004

Introduction

With continuing aircraft technology development over the last century, aircraft flying speeds have changed gradually from subsonic to supersonic and hypersonic speeds. Among the engine technologies used at these high speeds, the air-breathing ramjet has characteristics that include a simple structure, high load capacity, and no requirement for its own oxidizer, which means that this engine has become a research focus in hypersonic flight technology. Scramjets with flying Mach numbers of Ma 5–8 and $Ma > 8$ are usually called medium-range scramjets and high Mach scramjets, respectively. In the 1950s, Weber et al. performed a detailed analysis of the advantages and disadvantages of supersonic combustion [1]. Since then, there have been numerous research reports on scramjet engines. In the 1980s, NASA and the NASP jointly launched the Aerospace Plane Project, which verified the feasibility of scramjet engines [2,3]. In 1991, the Kholod aircraft carried out its first flight experiment and its flying Mach number reached 5.8 [4]. In 2004, the X43A completed a flight experiment with a Mach number of 9.6 [5,6].

The cross-sectional shapes of scramjets have undergone two transformations since their initial design, i.e., from circular to rectangular to circular. In the 1960s, because the internally rotating intake duct was more suitable for a transition to a circular cross-section combustion chamber and provided advantages in structural design, cooling and internal resistance, the circular cross-section combustion chamber was regarded as the ideal combustion chamber configuration [7]. In the 1980s, because wide-area flight requirements led to greater demand for variability in the combustion chamber geometry, and because the circular cross-section combustion chamber places higher requirements on fuel injection technology, scientific research units represented by NASP gradually turned their attention toward use of rectangular cross-sections [8]. In 1997, Aerojet adopted the circular dual-combustion ramjet (DCR) concept from the Johns Hopkins University Applied Physics Laboratory [9,10]. In 2002, Fred Billig and Aerojet Rocketdyne Holdings launched the Hyfly project and also used circular cross-section combustion [11]. The subsequent Hypersonic Collaborative Australia/United States Experiment (HyCAUSE) and Hypersonic International Flight Research Experimentation (HIFIRE) projects further confirmed that circular cross-section combustion chamber characteristics enable solution of the boundary layer problem in the corner zone and provide superior lift-drag after aircraft integration. The application of struts also means that the fuel injection problem has been solved preliminarily [12–16]. Therefore, the circular cross-section combustion chamber has once again become the preferred option for aspirated scramjets.

To provide the experimental data required for hypersonic vehicle design, it is important to obtain experimental internal flow field data; however, in hypersonic measurements using a direct-connected combustion test bench, the complex and harsh flow field environment inside the scramjet engine makes it difficult to apply invasive measurement methods to internal flow diagnosis. Noncontact optical measurement methods have therefore become particularly important. In previous experiments, many optical testing methods have been applied successfully. Willert et al. used particle image velocimetry (PIV) to measure the speed in the combustion chamber under both normal pressure and high-pressure environments, thus confirming the feasibility of PIV application in high-temperature combustion environments [17]. An et al. used high-speed photography techniques to analyze the effects of the ignition energy and positional changes on the cavity ignition process [18]. Planar laser-induced fluorescence (PLIF) is also used widely to measure OH and CH distributions in the incoming flow of the combustion chamber and the combustion field, along with the disturbance distribution in the combustion field [19–23]. In the HIFiRE-2 project, tunable diode laser absorption spectroscopy (TDLAS) was used to measure the composition at the combustor outlet [24,25]. In summary, the optical measurement experiments described above often required large measurement windows, but measurement methods that involve cutting out large optical measurement windows are not conducive to practical use in circular cross-section combustion chambers or actual flight experiments.

In this article, a test method for diagnosis of both the flame structure and the incoming flow state in a circular combustion chamber with a 100 mm inner diameter was performed using a pulse-type direct-connection combustion test bench. Twelve threaded holes with 8 mm inner diameters were excavated on the combustion chamber wall and combined with near/mid-infrared (1.4 μm and 2.5 μm) absorption spectrometry to measure dynamic changes in the flowing water content and a multi-view synchronous imaging method to study changes in the flame structure. Additionally, proper orthogonal decomposition (POD) was introduced to analyze the stability of the high Mach number combustion flame.

Experimental equipment

Detonation-driven direct-connected scramjet test facility

To perform scramjet ground experiments, it is necessary to obtain airflow that meets specific speed, temperature, and pressure requirements. The traditional electric heating method is clean and pollution-free, but its heating efficiency is low, and the slow speeds obtained can no longer meet the various indicators required simultaneously [26,27]. In 1957, Bird proposed the detonation drive concept [28]. In 1988, Yu proposed addition of a detonation section at the end of the driving section to eliminate the danger caused by the reflected ultra-high pressure and the interference with the downstream experimental airflow, thus allowing this low-cost driving method to be used to generate high enthalpy, high-pressure experimental airflow [29–32].

As shown in Fig. 1(a), the experiment was carried out on the JF-24 detonation drive platform of the Institute of Mechanics of the Chinese Academy of Sciences. The shock tube component comprises three sections: a driven section, a drive section, and a detonation section, with lengths of 7.5 m, 13 m and 2.5 m, respectively. The inner diameters of the driven section and drive section are both 130 mm, while the detonation section's inner diameter is 260 mm. The experimental section is a directly-connected combustion chamber with a

cavity flame stabilization structure, as shown in Fig. 1(b). When the equipment is running, the hydrogen-oxygen mixture in the driving section detonates through the diaphragm between sections Analysis of results and Analysis of hypersonic flame structure and pulsation characteristics, and the air pressure in the third section increases sharply. Eventually, the diaphragm between sections Experimental equipment and Analysis of results ruptures; this causes formation of a total experimental airflow with a total temperature of 3000–6000 K and total pressure of 5–20 MPa.

Before the experimental parameters are determined, it is necessary to carry out the simulation of the hypersonic inlet for given flight Mach number and flight altitude, as well as the design of the experimental parameters of the high enthalpy detonation-driven wind tunnel platform [33]. Through the simulation of the inlet, the airflow velocity at the entrance of the combustion chamber corresponding to the flight Mach number 10 is Mach 4.3. Then set the parameters of the test bench so that the test airflow with the same parameters is generated. After the parameter matching is completed, the actual measured total pressure and static pressure change curves of the experimental airflow are shown in Fig. 2. In addition, the experimental section in this article is a direct-connected combustor which does not include the inlet.

The total combustion chamber section length is 0.518 m and the cavity's inner diameter is 0.14 m. In this work, two injection methods are designed using the same number of injection holes: wall injection (WI) and cantilevered strut injection (CSI). WI relies on a circle comprising 12 wall injection holes with inner diameters of 1.0 mm that are evenly distributed perpendicular to the axial direction. CSI requires installation of four cantilevered struts with heights of 20 mm, widths of 10 mm and injection holes with an inner diameter of 1 mm at the top of the strut every 90°, rather than the four original injection holes in the wall. At this stage, there are eight wall injection holes and the four CSI holes are injected simultaneously. These two injection schemes were selected for this work and their specific working conditions are shown in Table 1.

Optical measurement system

Multiple pressure measurement points are arranged along each section of the experimental platform. In addition, the

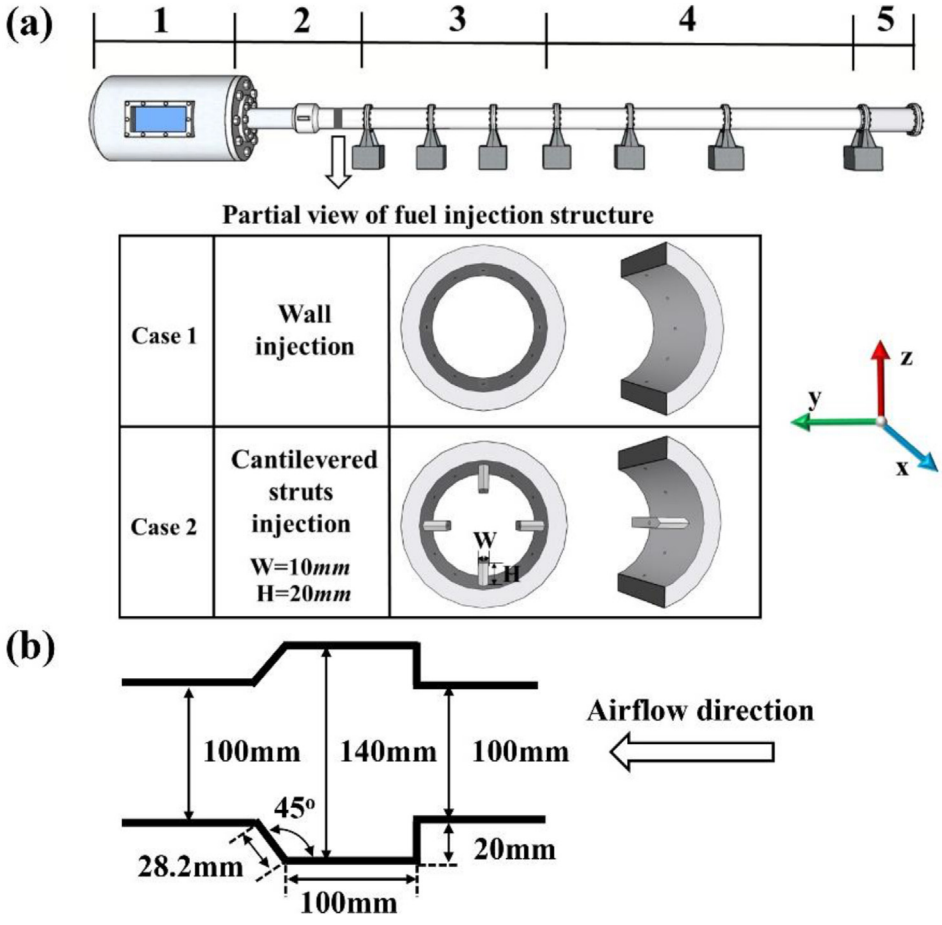

Fig. 1 – (a) High enthalpy detonation-driven wind tunnel platform and schematic diagram of fuel injection structure. 1: Vacuum tank; 2: High Mach number scramjet combustion chamber; 3: Driven section; 4: Drive section; 5: Unexploded section. The table shows schematic diagrams of two fuel injection structures, numbered Case 1, and Case 2. (b) Cavity section and sizes.

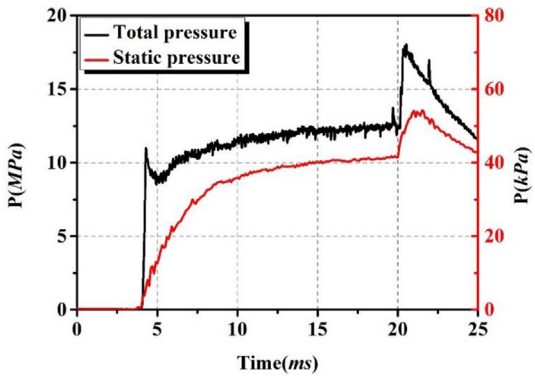

Fig. 2 – The total pressure and static pressure change curve of the experimental airflow.

combustion chamber is arranged to have heat flow measurement points along with optical measurement systems, including multi-view imaging sensors, TDLAS and photodetectors. All measurement systems use a digital delay generator (DG535, SRS) with time resolution of 5 ps to achieve high-precision simultaneous measurements using the test bench.

In previous studies, TDLAS technology has been used to measure the temperature, velocity, composition, and other properties of flow fields [34–36]. In this experiment, three laser control modules and three distributed feedback lasers (7185 cm^{-1}, 7444 cm^{-1}, 4030 cm^{-1}), a fiber splitter and a photodetector constitute an absorption spectrum measurement system [37], which is used to compare the sensor data and thus assist in determining the effective time of the experimental gas. The TDLAS system's repetition rate is 10 kHz.

The multi-view imaging system is composed of a 1 × 6 imaging fiber bundle-coupled high-speed camera (FASTCAM SA-Z), and each angle-of-view has a field of view of 50°. This system greatly simplifies multi-view imaging and provides strong assembly adaptability characteristics and cost savings. This imaging system has been used in optical diagnosis of swirling combustion flames [38,39] and successfully obtained multiple views of complex flame structure projections. As shown in Fig. 3, the six lenses of the imaging system are divided into two groups; one group of four is distributed evenly at one end of the cavity and spaced 90° apart, while the other two are placed horizontally on the cavity wall and form an angle of 45° with the Y-axis of the coordinate system in Fig. 1. In Fig. 4(a), the lenses are numbered Lens 1–6. To show the imaging area more intuitively, the cavity's upstream, inner, and downstream areas are labeled A, B and C, respectively, in Fig. 4(b) and the corresponding areas are filled using different patterns. The imaging area of Lenses 1–4 is mainly within area A and part of area B, the imaging area of Lens 5 is mainly in area B and part of area A, and the imaging area of Lens 6 is mainly in area B and part of area C.

In addition, a photodetector with a bandwidth of 11.7 MHz (DET20C2, Thorlabs) is installed at the combustion chamber exit to record changes in the light intensity in area C and to assist in determining the real-time positional information of the flame.

Table 1 – Experimental conditions.

Experiment number	Case 1	Case 2
Injection method	12 WI	8 WI+4 CSI
Mach	10	10
Flight altitude	34 km	34 km
Equivalence ratio	1.0	1.0
Injection pressure	6.7 MPa	6.7 MPa
Total temperature	3800 K	3800 K
Total pressure	12 MPa	12 MPa

Analysis of results

The effective experimental time of the scramjet experiment based on the pulsed detonation shock wave wind tunnel platform is of the order of only milliseconds. In addition, when the driving gas passes through the bifurcation area formed by the incident shock wave near the shock tube wall, it will form early pollution of the test gas [40,41], which means that it is particularly important to define the effective time of the experiment. In our experiment, the water vapor content of the driving gas after detonation of the hydrogen and oxygen mixture is higher than that of the experimental gas, and thus detection of the water content in the gas flow has become a feasible method to determine whether the incoming flow meets the demand.

In this experiment, the TDLAS measurement system is used to detect the water pressure of the airflow quantitatively, and has measurement uncertainty of less than 3% [42,43]. Fig. 5(a) shows the background emission received by the detector of the TDLAS system in multiple experiments. The first strong step signal is generated due to the arrival of the shock wave, which shows that the experiment has good repeatability. As shown in Fig. 5(b), the red line represents the static pressure curve obtained using the wall pressure sensor (NS-3, Zemper Automation) when the experimental airflow reaches zone 2 in Fig. 1 and the black line represents the water pressure curve obtained via TDLAS.

After the driven gas in zone 3 reaches the combustion chamber at 5 ms, the static pressure of the driven gas flow obtained via the wall pressure sensor begins to increase before gradually stabilizing at approximately 10 ms. Simultaneously, the TDLAS measurement system detected the increase in the water content rapidly, but the water was mainly concentrated near the wall at this time and had little effect on combustion [44]. When the time approaches 14 ms, the water pressure curve suddenly rises sharply. This occurs because the driving gas, which is doped with the hydrogen-oxygen reaction product of water, reaches the combustion chamber. At this time, the test gas is no longer the required air, which means the end of the experiment. Although the pressure data indicated by the red curve maintained a stable time period of approximately 8 ms after 14 ms, the experimental gas no longer met the experimental requirements during this period. The reflected shock wave reaches the measurement point in the combustion chamber at 23 ms, which causes the airflow to be compressed again, and the water pressure signal shows a rapid jump. However, the pressure sensor's response is relatively slow and we believe that the pressure sensor's response

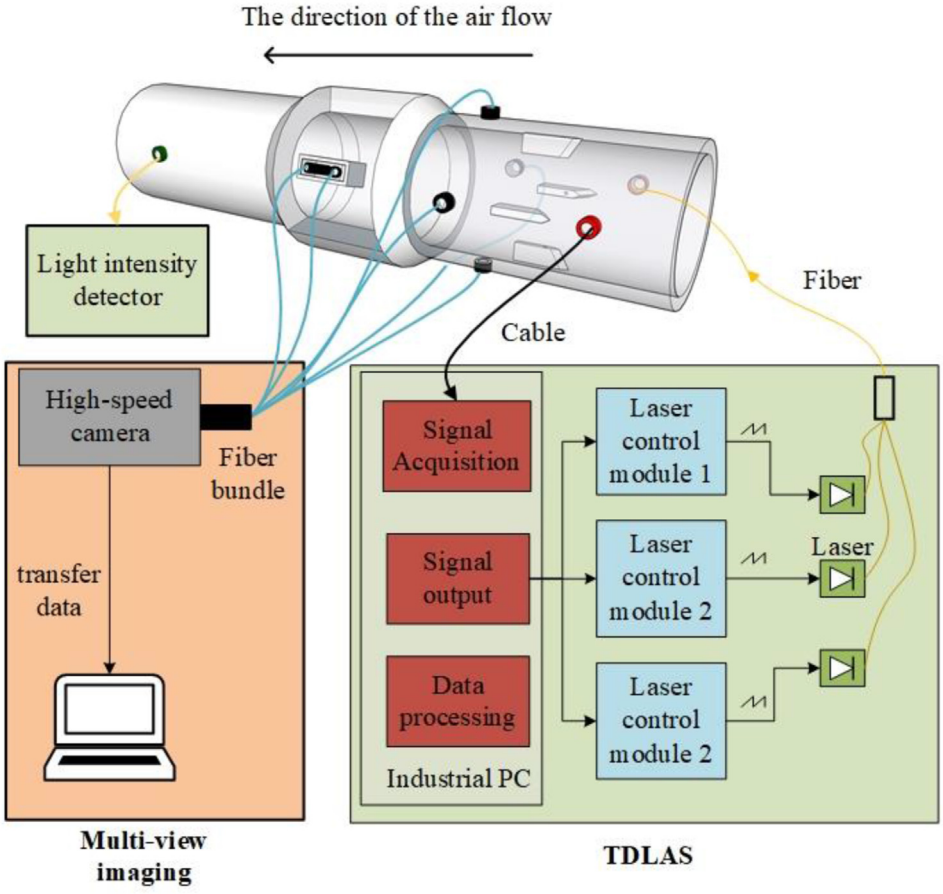

Fig. 3 – Schematic diagram of installation of multi-view imaging system, absorption spectrum measurement system and light intensity detection equipment.

frequency is insufficient to display the appearance time of the pressure platform correctly. In other words, the static pressure should have reached a relatively stable state before 10 ms. In this experiment, we select 8 ms, which shows more than 50% of the average static pressure, as the starting point for the effective experimental time.

Traditional flow field display methods such as schlieren methods have stricter window requirements and make it difficult to perform this experiment. Instead, we used an optical diagnosis method that combines small holes in the wall with multi-view high-speed simultaneous imaging. As a flow display method with high time resolution and a wide sampling range, high-speed photography is highly suitable for scramjet ground experiments. In this experiment, the fiber bundle multi-view simultaneous imaging method was used to record the radiation grayscale image, including both chemiluminescence and particulate high-temperature radiation, and a more comprehensive millisecond-level flame structure change image was thus obtained at a sampling rate of 20,000 Hz. Figs. 6 and 7 show the pseudo-color processing results from multi-view imaging of specific time nodes of Cases 1 and 2, respectively. The color bar parameters represent the relative combustion intensities. Smaller numbers indicate weaker flames, while in contrast, larger numbers indicate more intense burning. The exposure times for Figs. 6 and 7 are 1/800 ms and 1/160 ms, respectively. For the time point changes, we used A1–A20 to number the displayed images and the arrangement of Lens 1–6 is shown in Fig. 4(b).

The detonation drive uses the high-pressure gas produced by detonating the combustible mixture as the driving gas to generate the incident shock waves. The incident shock wave then compresses and heats the gas in the driven section, and the diaphragm at the end of the driven section finally ruptures. The high-pressure gas generates a starting shock wave under the low-pressure condition at the nozzle. Images A1–A5 in Fig. 6 show the optical radiation effects that result from the shock waves caused by rupture of the diaphragm between zones 2 and 3 when the pressure in zone 3 reaches a critical value. The shock wave in A1 has just reached the measurement point positions of Lenses 1–4 and only half of the viewing angles are illuminated at this instant. These four viewing angles are fully illuminated in A2 after 0.05 ms. Because the optical axis of Lens 6 is at 45° to the positive direction of the Y-axis in Fig. 1, it is illuminated first. As the shock wave continues to move downstream, Lens 5, which has an optical axis oriented at 45° to the negative direction of the Y-axis in A3, is also illuminated. In A6 (8 ms), the shock wave and the high-temperature non-equilibrium gas after the wave have both passed through completely and the effective experimental airflow has been established. At this time, the

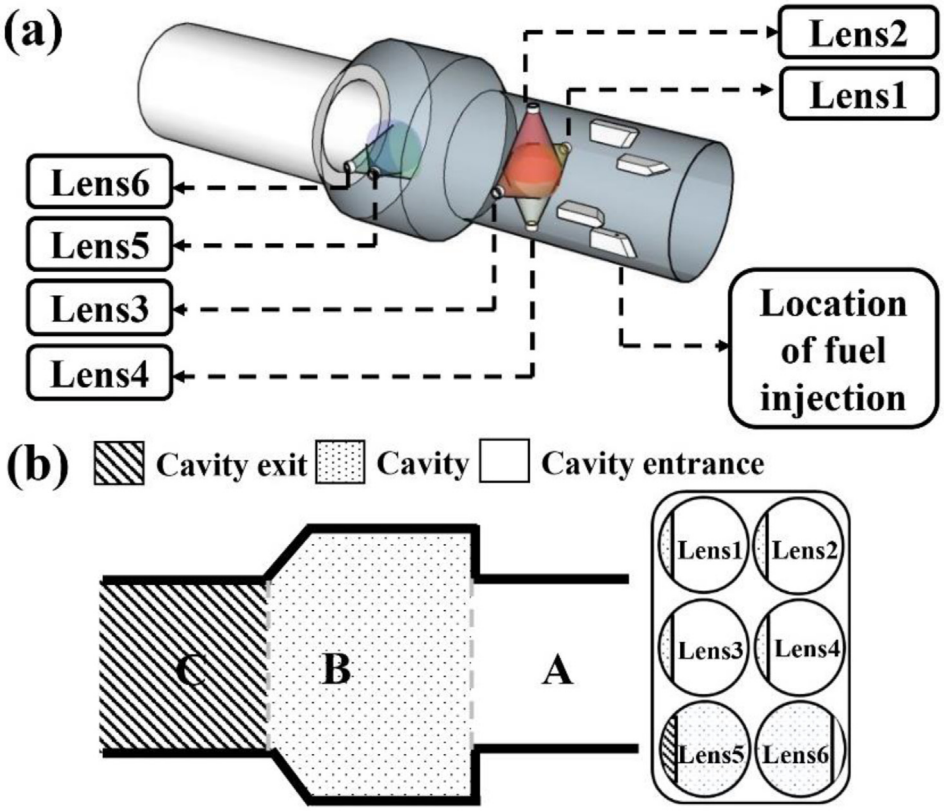

Fig. 4 – (a) Positions of each lens for multi-view imaging. (b) Imaging areas of each lens and arrangement of imaging results on the pixels.

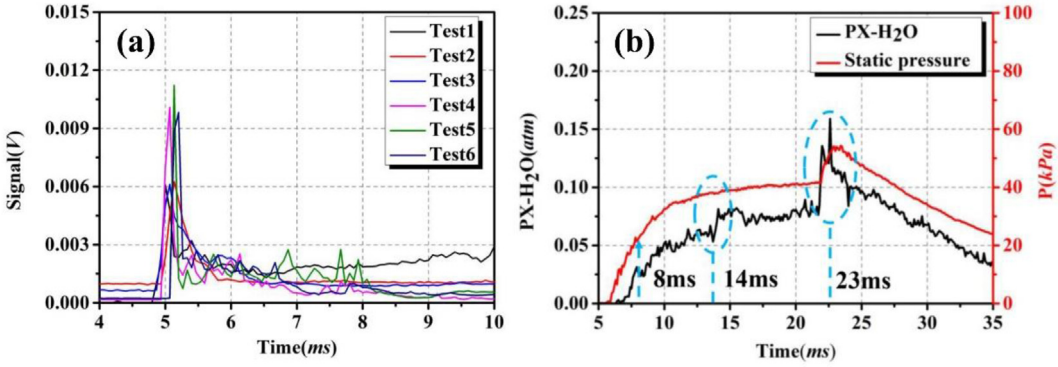

Fig. 5 – (a) The background emission intensity received by the TDLAS system at different tests (b)The red line is the change curve of the experimental airflow static pressure and the black line is the water pressure in the experimental airflow. The points marked with the blue lines are, from left to right, the starting point, the end point, and the reflected shock wave arrival time. (For interpretation of the references to color in this figure legend, the reader is referred to the Web version of this article.)

response intensity of each optical measurement device is reduced. Images A1–A5 in Fig. 7 also show detection of the flow field establishment process.

Ignition methods for scramjets mainly include forced ignition and self-ignition. The self-ignition method involves direct ignition of the mixture when the total engine inlet temperature is high and the flying Mach number is high [45,46]. As described in section Detonation-driven direct-connected scramjet test facility, because the total temperature of the driven airflow increases significantly after the shock wave, the self-ignition mechanism takes effect after fuel injection. In this experiment, the two injection methods achieved self-ignition successfully after fuel injection at 8 ms. Images A6–A8 in Fig. 6 and A6–A8 in Fig. 7 show that the flame is first generated in the upstream area of the cavity (zone A in Fig. 4) before gradually developing into the cavity (zone B in Fig. 4). Images A11–A15 in both Figs. 6 and 7 show that when the flame in zone A remains relatively stable,

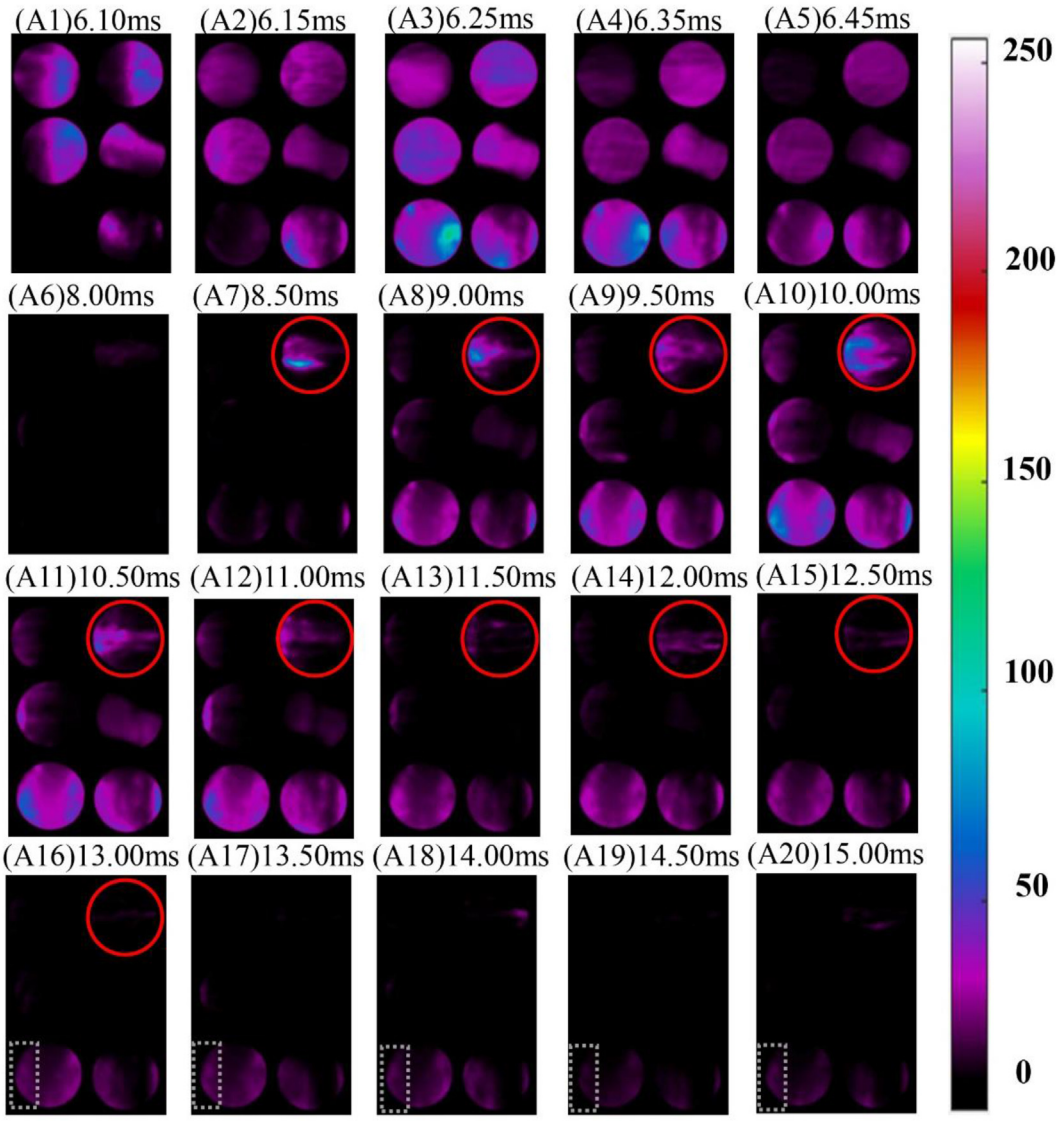

Fig. 6 – (Case 1) Multi-view flame images of some of the time nodes during injection of 12 wall holes. Red circles indicate the flame characteristic structures captured by lens 2 and the gray dashed lines indicate the junction of zone C and zone B in Fig. 4. (For interpretation of the references to color in this figure legend, the reader is referred to the Web version of this article.)

burning with a weaker radiation intensity also occurs in zone B. The difference between the two sets of experiments is that Case 1 produced a flame with a more obvious flocculent characteristic, as indicated by the red circle in Fig. 6, while Case 2 produced an approximately columnar flame, as indicated by the red circle in Fig. 7.

It is not difficult to determine that a specific experimental phenomenon is involved here, because Lenses 1, 2, 3, and 4, as shown in Fig. 4, are uniformly installed 90° apart around the circumference of the section. Because the distributions of the injection holes and the cantilevered struts are uniform and the injection pressure remains the same, the collected images should theoretically have a high degree of symmetry. However, as shown in images A7–A16 in Fig. 6 and A7–A20 in Fig. 7, only Lens 2 has captured the complete flame structure, while Lenses 1, 3 and 4 did not capture the characteristic flame shape mentioned above. This shows that the flame adheres to the lower wall at the junction between zones A and B in Fig. 4(b) for a long time, and this zone lies in the blind zones of Lenses 1, 3 and 4. The cause of this phenomenon requires in-depth study. We believe that one possible cause may be that a small amount of particulate matter that has been deposited on the lower wall of the pipe after multiple experiments reaches higher temperatures after being heated, which may then promote burning. Because of particulate matter deposition, the window in which Lens 4 is installed is also partially covered and its image is incomplete, as Fig. 6 shows.

The intensity of the camera's response is directly related to the radiance. However, chemiluminescence and particle luminescence are hardly to tell apart completely during flame imaging which are well used in scramjet ground tests. Fortunately, these two radiation mechanisms both reflect the high-

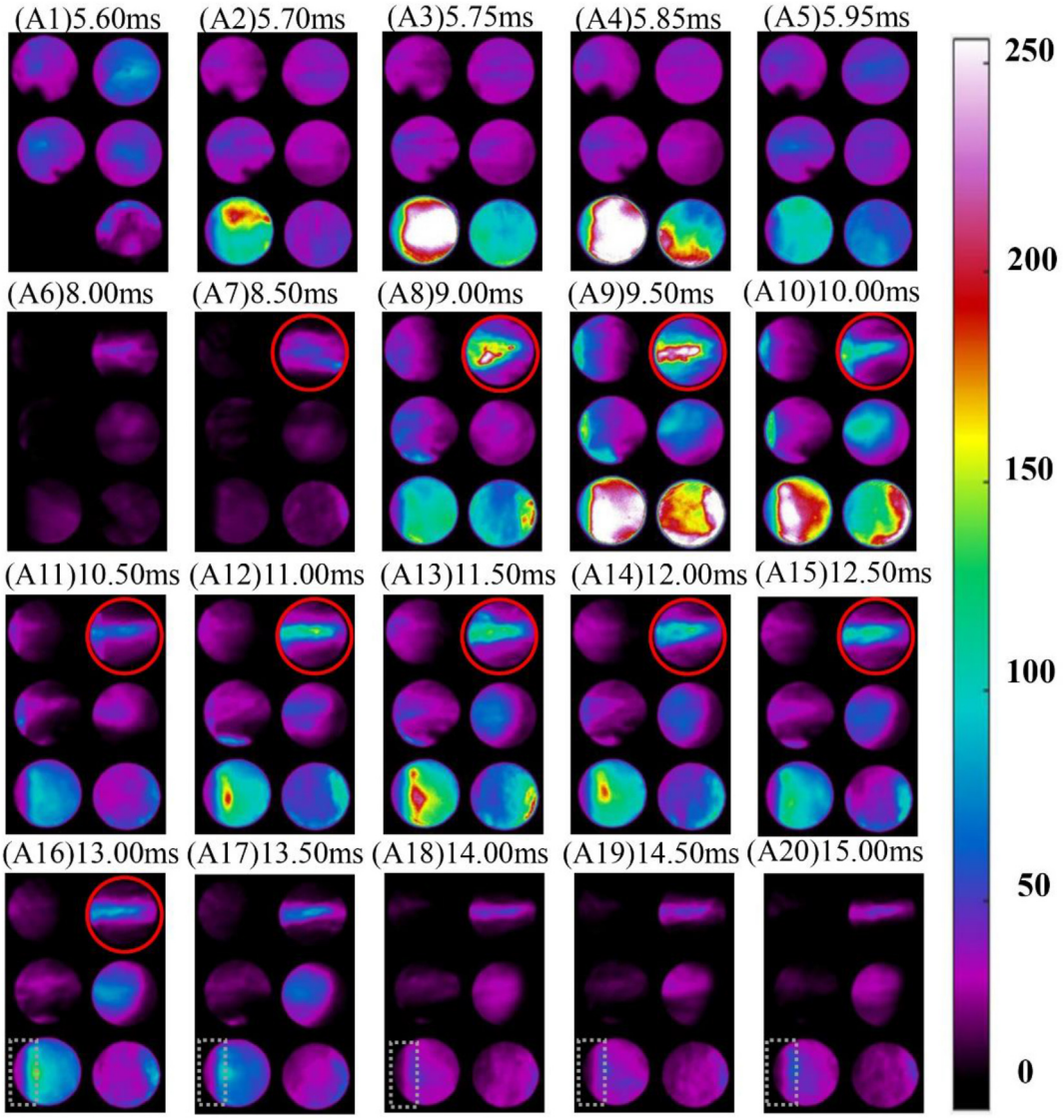

Fig. 7 – (Case 2) Multi-view flame images of some of the time nodes during injection of eight wall holes and four cantilevered strut holes. Red circles indicate the flame characteristic structures captured by Lens 2 and gray dashed lines indicate the junction of zone C and zone B in Fig. 4. (For interpretation of the references to color in this figure legend, the reader is referred to the Web version of this article.)

temperature caused by the chemical reaction in the high-speed turbulent flow. Therefore, we believe that the gray value obtained from radiation imaging in current study is suitable for use in judging both the flame structure and the combustion oscillation. In the future, we will further study the radiation spectrum which can proved more information especially in quantitative cases [39]. Although quantitative data are not currently available, the time changes in relative intensity are still very useful in combustion analysis. The normalized intensity changes curves for the flame radiation intensity inside the cavity (zone B in Fig. 4(b)) and upstream of the cavity (zone A in Fig. 4(b)) from the two sets of experiments for Case 1 and Case 2 obtained using the multi-view imaging system are shown in Fig. 8.

In Fig. 8, the blue dotted line and the red solid line represent the normalized radiation intensities inside the cavity (zone B in Fig. 4) and upstream of the cavity (zone A in Fig. 4), respectively. The two sets of red and blue curve comparison diagrams roughly illustrate the development processes of the shock wave as it passes through and the flame in the combustion chamber from ignition to extinction in the experiments, respectively. At approximately 6 ms, the radiation intensity curves for the two sets of experiments in Fig. 8 all showed a large rise and fall related to the passage of the shock waves and establishment of the flow fields. In the subsequent period from 8 ms to 13 ms, the total temperature and total pressure of the incoming flow were both high, which resulted in a violent and high Mach number flame. Although the fuel injection method is different, combustion occurs in the cavity, which shows that the cavity structure in the circular-cross-section scramjet combustion chamber plays a significant role in stabilizing the flame and promoting combustion.

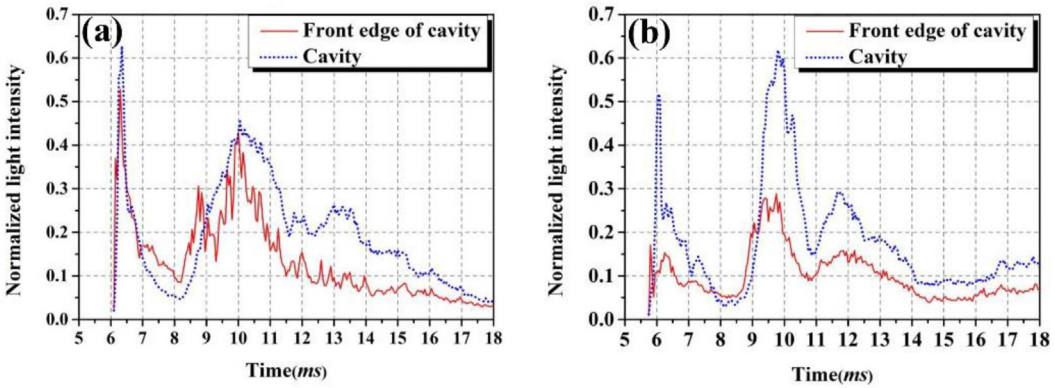

Fig. 8 – (a) (b) are flame combustion intensity change curves of Case 1 and Case 2,respectively. The solid red line represents the inside of the cavity front edge (A zone) and the blue dotted line represents the interior of the cavity (B zone). (For interpretation of the references to color in this figure legend, the reader is referred to the Web version of this article.)

Fig. 9(a) and (b) show the normalized light intensity response curves from the two measurement points in Case 1 and Case 2, respectively. The red and blue lines represent the light intensity signals from the light intensity detector and TDLAS, respectively. As indicated by the blue dotted line, the responses of these two sets of equipment are not synchronized. This is because the measurement point of the light intensity detector is located approximately 1.0 m downstream from that of the TDLAS system along the airflow direction, causing the response take-off points to lag behind by approximately 0.8 ms. As the radiation intensity curve in Fig. 8 shows, the experimental flame began to extinguish at 13–18 ms and the radiation intensity dropped sharply. However, as shown in Fig. 9(a), the signal intensity curve of the light intensity detector downstream of the cavity in Case 1 has a gentle slope. In addition, the slope of the signal drop curve for the light intensity detector in Case 2 shown in Fig. 9(b) is basically the same as that inside and upstream of the cavity.

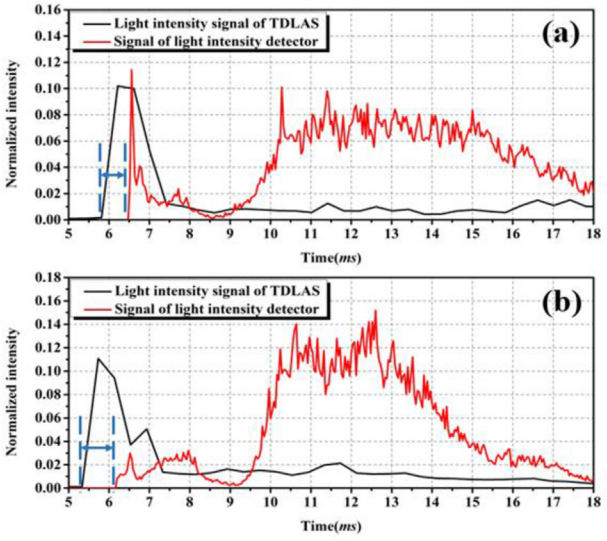

Fig. 9 – In (a) Case 1 and (b) Case 2, the red and black curves show the light intensity response changes of the light intensity detectors and TDLAS, respectively. (For interpretation of the references to color in this figure legend, the reader is referred to the Web version of this article.)

In scramjet design and research, the sufficient and concentrated combustion state in the combustion chamber is an important factor for evaluation of the superiority of the proposed fuel injection structure. The areas marked using the small gray rectangles in images A16–A17 in Figs. 6 and 7 form part of the downstream area of the cavity, as captured using Lens 5 (zone C in Fig. 4). There is no obvious dividing line in this area in images A16–A20 in Fig. 6. It can also be seen that flames appeared downstream of the cavity. In Fig. 7, a clear dividing line in this area is shown in images A16 to A20, the radiation intensity in the cavity is higher than that downstream of the cavity, and the downstream area of the cavity becomes darker over time. Therefore, the flame was not completely extinguished after 13 ms in Case 1, but subsequently moved downstream into the cavity. The presence of the cantilevered struts in Case 2 leads to a low-speed zone and the flame generated by injection from the cantilevered struts forms a pilot flame, which then causes the fuel to burn more fully in the cavity. Pandey et al. also found that the combination of a support plate and wall injection helps to improve mixing of the fuel and the air to enhance combustion [46–48]. From the pressure data along the test bench obtained from the experiment, we also found that the existence of cantilevered struts helps to enhance the pressure rise in the combustion chamber, indicating a higher heat release rate in the combustion chamber. Therefore, it is determined that, under the same injection pressure, flow rate and equivalence ratio conditions, addition of part of the cantilevered strut injection structure can cause the fuel to burn fully and intensely.

Analysis of hypersonic flame structure and pulsation characteristics

Unsteady supersonic combustion processes generally exist in scramjet combustors. Separation of the supersonic boundary layer is often accompanied by low-frequency oscillations. In

some cases, this flow instability will become the dominant supersonic combustion instability mechanism. Effective control of unsteady supersonic combustion is an important measure for practical scramjet use [49,50]. In addition to obtaining the structural characteristics of the flame, multi-view imaging can also be used to analyze the flame pulsation frequency characteristics with the added advantage of high-frequency measurement.

The combustion instability is caused by interactions among the heat release rate fluctuations, acoustic oscillations, and flow and mixing process fluctuations. The interior of the engine's combustion chamber can be regarded as a self-excited oscillation system. The heat generated by combustion provides energy for the system, which leads to a continuous oscillation process. It is generally believed that downstream disturbances in supersonic airflow cannot propagate to the upstream area, but there are in fact subsonic regions inside scramjets, including the boundary layer, the main recirculation zone, and the angular recirculation zone. Therefore, there may be closed-loop feedback between the sound waves and the heat released inside the scramjet. Use of the cavity on the wall reduces the total pressure loss of the incoming flow significantly, but different incoming Mach numbers and the cavity aspect ratio also cause different degrees of self-excited oscillation in the cavity [51,52]. *Ma* et al. pointed out that combustion oscillations occur in the dual-mode scramjet. The oscillation frequency ranges were 100–160 Hz for liquid JP-7 fuel and 300–360 Hz for gaseous ethylene fuel [53]. Micka et al. studied the combustion stabilization characteristics in the combustor of a dual-mode scramjet with a cavity and found that the flame front oscillated between the jet wake area and the cavity [54,55]. Li et al. performed experimental research on the combustion oscillation phenomenon in the combustor of a dual-mode scramjet using high-speed schlieren imaging, CH* self-luminescence imaging and TDLAS. Their results showed that the flame oscillated greatly between the upstream cavity and the downstream cavity with an oscillation frequency of approximately 50 Hz [56].

Lumley introduced proper orthogonal decomposition (POD) into the turbulence research field, thus providing researchers with an effective mathematical analysis method and concept [57]. Dynamic flame images can also be used to analyze the dynamic characteristics and pulsation mechanisms through statistical data mining techniques. POD analysis is an unsupervised cluster analysis method that converts the original image into modal data, classifies the flame pulsation situation, and subsequently obtains the pulsation modalities and the related time series of the image data [58–60]. To enable further analysis of the spatial pulsation characteristics of the coupling between high Mach number flames and high-speed flows, we perform POD analysis on high-speed photography images. The basic idea of POD is to assume that the continuously changing flame images can be linearly superimposed using multiple orthogonal modalities.

$$A(x,t)=\sum_{i=0}^{M}\alpha_i(t)\phi_i(x) \tag{1}$$

where $\boldsymbol{X}$ represents the spatial coordinate (pixels), $\boldsymbol{t}$ represents the time coordinate, α_i represents the time coefficient of the mode, ϕ_i represents the spatial distribution characteristics of the mode and $\boldsymbol{M}$ represents the number of modes. As discussed in section Analysis of results, because of particle coverage and combustion asymmetry, only some of the lenses collected relatively complete flame images; we therefore only use the images collected by Lens 2 to observe the flame pulsation.

An image containing $\boldsymbol{W}$ pixels in each row and $\boldsymbol{L}$ pixels in each column can form a pixel matrix of $\boldsymbol{m}=\boldsymbol{L}\times\boldsymbol{W}$. Therefore, $\boldsymbol{n}$ images can be expressed as the $\boldsymbol{m}\times\boldsymbol{n}$-dimensional data matrix AA, which can be decomposed into the product of three matrices via singular value decomposition (SVD):

$$A_{m\times n}=U_{m\times m}S_{m\times n}V^{T}_{n\times n} \tag{2}$$

In Eq. (2), $\boldsymbol{U}$ represents the spatial distribution of the different modes, $\boldsymbol{S}$ represents the pulsation energy of the different modes, and $\boldsymbol{V}$ represents the time distribution of the different modes. To solve for the three matrices of $\boldsymbol{U}$, $\boldsymbol{S}$ and $\boldsymbol{V}$, we use snapshots [61] to transform Eq. (2) as follows:

$$A^{T}A=VS^{2}V^{T} \tag{3}$$

We then multiply the right of Eq. (3) by $\boldsymbol{V}$ and substitute $S=\sqrt{\lambda}$ to obtain:

$$A^{T}AV=VS^{2}=V\lambda \tag{4}$$

At this time, $\boldsymbol{V}$ and $\boldsymbol{S}$ can be obtained by solving for the eigenvectors and eigenvalues of $\boldsymbol{A^{T}A}$, and then solving for $\boldsymbol{U}$ using $\boldsymbol{U}\times\boldsymbol{S}=\boldsymbol{A}\times\boldsymbol{V}$. The ***i-th*** column of matrix $\boldsymbol{U}$ is the spatial distribution of mode $\boldsymbol{i}$. The ***i-th*** column of matrix $\boldsymbol{V}$ multiplied by the ***i-th*** value of matrix $\boldsymbol{S}$ gives the time coefficient α_i of mode $\boldsymbol{i}$. If the eigenvalues λ are sorted from large to small, the modal pulsation energy at the top of the sequence is large and at the same time is dominant in the flame pulsation behavior, indicating that attention should be devoted to it in the analysis.

Fig. 10(a) shows the changes in $\boldsymbol{t}$ for the 0th mode and the first four modes during wall injection. The figure shows that the $\boldsymbol{t}$ values of the 0th mode are all negative, which means there is no difference in the spatial distribution for the overall change in the flame heat release rate. Although the time coefficients of the other fourth-order modes all show positive and negative alternation phenomena, they can be regarded as labels or weights assigned to the instantaneous original snapshots.

Fig. 10(b) shows the energy proportion for the tenth-order mode with the energy ranking at the top. As the order number increases, the modal energy decreases gradually, but the proportion of the first four modes reaches nearly 65%. Therefore, the next step must be to analyze the first four modes. In the same modal diagram, yellow and blue both represent areas with strong pulsation; the yellow areas represent areas where the burning becomes violent and the blue areas represent areas where the burning is weakening at the same time. In addition, the pulsation amplitudes of areas between yellow and blue areas are weaker. POD is a cluster analysis method and the extracted modal information cannot express a specific meaning by itself; the information must thus be analyzed in combination with knowledge and

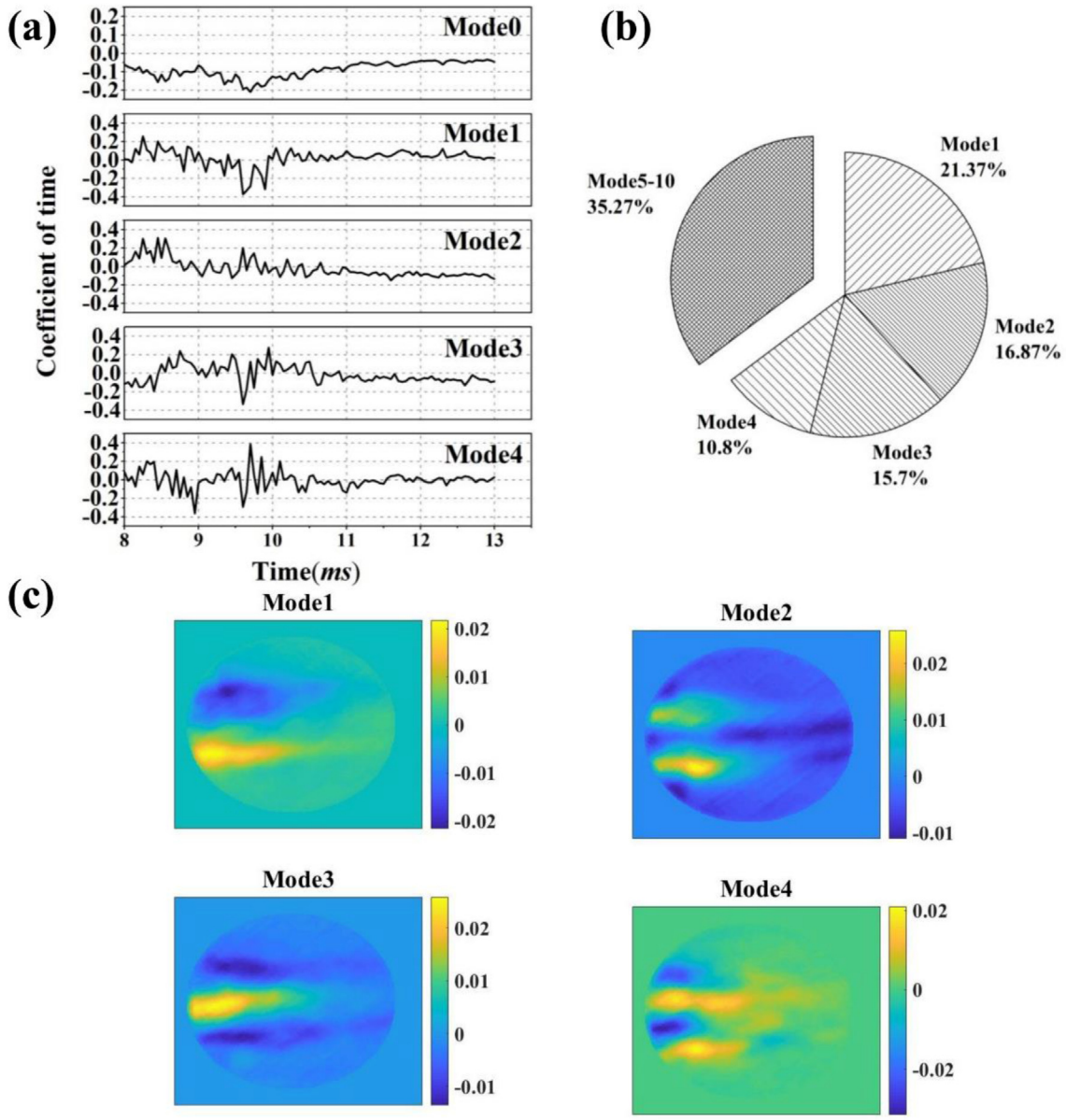

Fig. 10 – (a) t variation curves of the 0th mode and the first four modes in Case 1. (b) Energy ratio of the first ten modes (c) Pulsation of the first four modes.

experience of the flow and combustion fields. The strong pulsation area of mode 1 appears alternately on the two sides that deviate from the axis (in the coordinate system from Fig. 1 in the X-axis direction), which indicates that the oscillation situation that deviates from the axis is the main form of flame pulsation. This is probably related to the pressure rise caused by heat release in the combustion chamber, which caused a large boundary layer separation in the supersonic flow. Modes 2–4 show multiple strong pulsation areas that are related to wall injection of the fuel, thus indicating that the scattered flocculent flame structure is the main feature of the wall injection mode.

Fig. 11 shows the change curve for the time coefficient in Case 2 and the pulsation energy proportions of the first ten orders. Fig. 11 shows that the 0th-order mode still shows no spatial differences and that the top four modes among the top ten modes when ranked from high to low account for nearly 55% of the pulsation energy, and thus we still mainly analyze the first four modes. Mode 1 is very similar to the corresponding mode in Fig. 10(c). Two strong pulsation zones are distributed on both sides of the axis and the flame has a main pulsation that deviates from the axis. However, the cantilevered struts make the two strong pulsation zones more compact; this also confirms the columnar flame structure shown in Fig. 7. Modes 2–4 showed completely different characteristics from the wall injection modes, manifesting as an axial (y-axis in Fig. 1) oscillation mode. Therefore, the presence of the cantilevered struts has a major influence on the flame oscillation characteristics.

Many studies have confirmed the existence of low-frequency combustion oscillations caused by the strong interactions among the jet, the cavity flame stabilization zone,

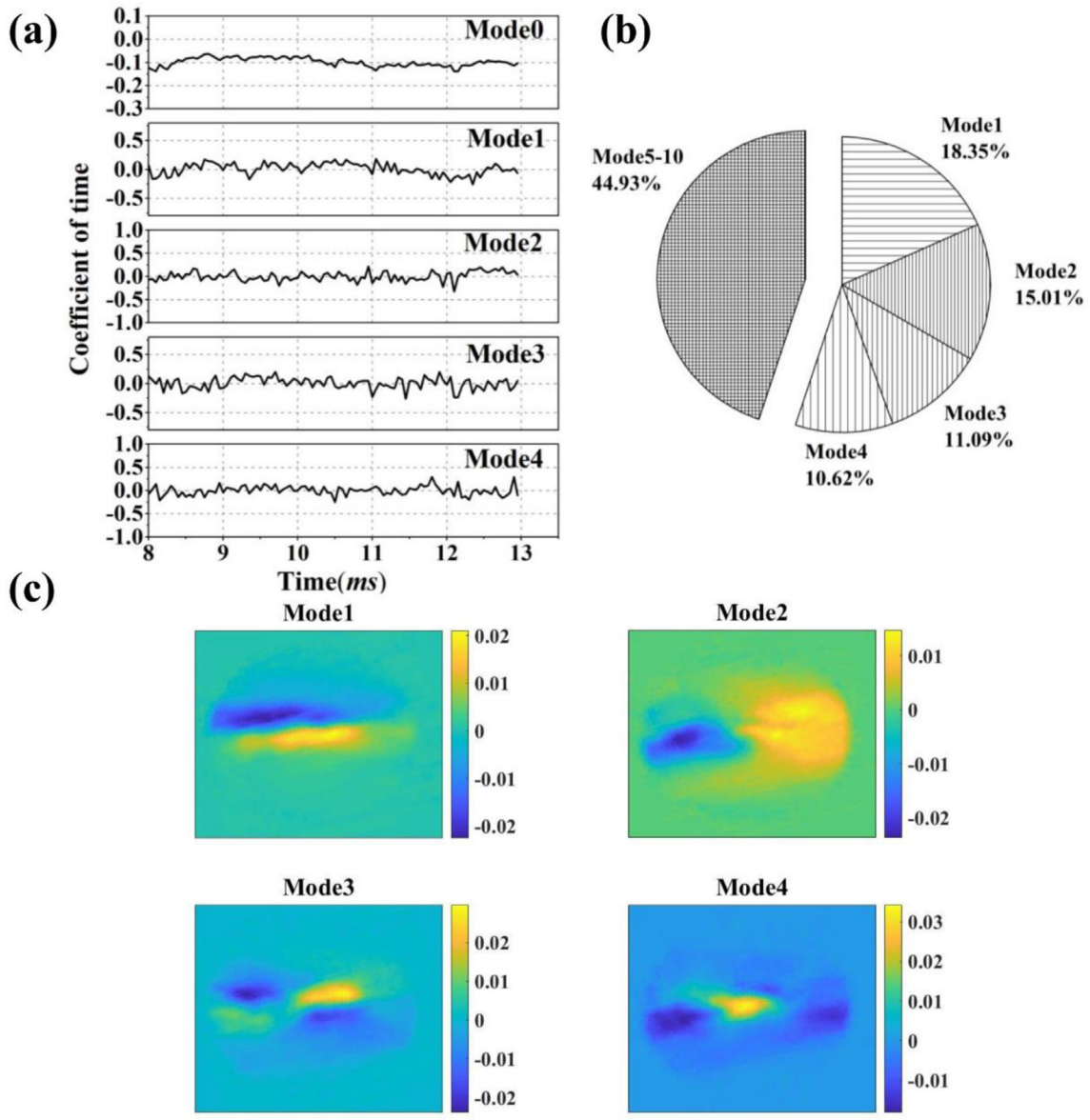

Fig. 11 – (a) t variation curve of the 0th mode and the first four modes in Case 2. (b) Energy proportions of the ten modes with the highest energy rankings. (c) Pulsation of the first four modes.

the mainstream combustion zone, and the pre-combustion shock train in scramjet engines [62–65]. In previous studies, methods such as Fourier transforms were commonly used as effective frequency analysis methods, but conventional Fourier transform methods cannot describe these frequency components at any time and cannot analyze them fully. The time-frequency joint analysis method represented by wavelet transforms can transform a one-dimensional time-domain signal into a two-dimensional time-frequency plane. This provides a multi-scale signal refinement to produce a multi-resolution analysis method that uses time subdivision at high frequencies and frequency subdivision at low frequencies. Wickersham et al. applied the wavelet analysis method to the flame holder experimental platform [66] and confirmed the feasibility of using wavelet analysis to extract flow and combustion characteristics. In this article, we attempt to select the average mode from the mode information extracted using the POD method for wavelet analysis.

The 0th-order mode is also called the average mode and is the average of all images. Wavelet analysis of the time coefficient variation curve of the 0th-order mode obtained via the POD analysis above can obtain the corresponding time-frequency analysis graph, as shown in Fig. 12, where the Pw (power spectrum) of the ordinate represents the wavelet power. As shown in Fig. 12, Cases 1 and 2 have full-time main frequency combustion oscillation ranges of 270–450 Hz and 280–550 Hz, respectively. The two injection methods have relatively close ranges in their main oscillation frequencies and thus the high Mach number combustion flame oscillation behavior of this type of circular cross-section combustor pulse

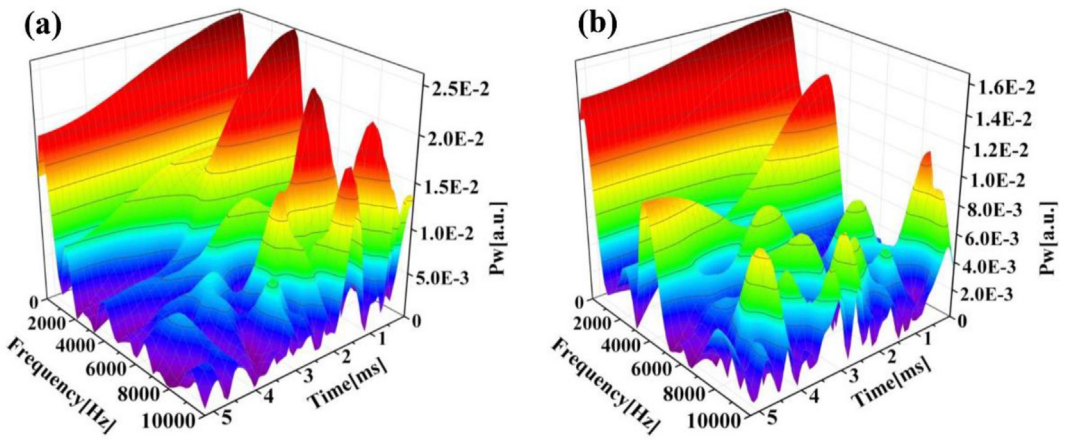

Fig. 12 – Time-frequency analysis diagrams of (a) Case 1 and (b) Case 2 based on the average mode.

test bench should be affected more strongly by flow instability when simulating flight Mach number 10. The combustion instability caused by the different fuel and air mixing levels that result from different injection methods is thus not the dominant factor in combustion oscillation.

Fleifil et al. found that the combustion process is limited by high-frequency disturbances, but it has a strong influence on low-frequency disturbances [67]. Fig. 12 shows that both Cases 1 and 2 have wide-ranging high-frequency oscillations in the 2–5 ms period, but the amplitudes of these oscillations are relatively small and their impact on the engine performance is also limited. Therefore, it will be necessary to improve the test bench running time to analyze the lower frequency combustion pulsations, and more attention must be paid to the low frequency interference problem in engine design.

Conclusion

Without using large-sized optical windows, a preliminary study of the internal flow field for a flying Mach 10 in the circular scramjet combustor was performed using optical measurement methods including TDLAS, emission intensity monitoring and high-speed multi-view imaging using a fiber bundle.

(1) In the hypersonic ground experiments, the effective experimental time is precious and is difficult to evaluate accurately using pressure sensors. Dynamic monitoring of the water concentration produced by hydrogen/oxygen detonation using TDLAS technology allows the effective experimental time to be determined to be 5 ms, which is 8 ms less than the value obtained via the pressure sensors.
(2) Multi-view imaging technology provides an intuitive demonstration of the process from flame self-ignition to violent combustion and extinction within milliseconds. The flame structures showed flocculent and columnar characteristics for the two different injection methods and the presence of the cantilevered struts played a role in supporting combustion.
(3) On the basis of high-frequency flame image acquisition and through application of POD, it is found that the flames under the different working conditions show high-frequency oscillations at the beginning of ignition and full-time main frequency combustion oscillations.

Funding

This work was supported by: The National Natural Science Foundation of China [grant numbers 12072355, 11802315, 11927803]; and the Youth Innovation Promotion Association of CAS [grant number 2018023].

Declaration of competing interest

The authors declare that they have no known competing financial interests or personal relationships that could have appeared to influence the work reported in this paper.

Acknowledgments

The authors thank *Prof. Wang Chun, Mr. Dongdong Meng, and Dr. Qifan Zhang* et al. for their guidance in performing the experiments and analysis of the results. We thank David MacDonald, MSc, from Liwen Bianji, Edanz Editing China (www.liwenbianji.cn/ac), for editing the English text of a draft of this manuscript.

REFERENCES

[1] Weber RJ, Mackay JS. An analysis of ramjet engines using supersonic combustion. Technical Report Archive & Image Library; 1958.
[2] Tank MH. National aero-space Plane (NASP) program [R]. NASA-N91-28214. 1991.
[3] Augenstein B, Harris E, Aroesty J, et al. The national Aerospace Plane (NASP): development issues for the follow-on vehicle [M]. RAND Corporation; 1993. R-3878/1-AF.

[4] Roudakov A, Schickhman Y, Semeov V, Novell Ph, Fourt O. Flight testing an axisymmetric scramjet: Russian recent advances. International Astronautical Federation; Oct 1993. IAD Paper 93-S.4.485, 44th.

[5] Holland SD, Woods WC, Engelund WC. Hyper-X research vehicle experimental aerodynamics test program overview. J Spacecraft Rockets 2001;38(6):828–35.

[6] Freeman Jr DC, Charles RMC, Vincent LR, et al. The NASA hyper-X program. 1997.

[7] Siebenhaar A, Bogar T. The impact of round combustors on TBCC propulsion and hypersonic cruise vehicles. In: 14th AIAA/AHI space planes and hypersonic systems and technologies conference; 2006. https://doi.org/10.2514/6.2006-7986.

[8] Simmons J, Weidner E. Design of scramjet inlets with rectangular capture cross-section and circular throat. NASA TM; 1986. p. 87752.

[9] Kuo KK, Chiaverini MJ, editors. Fundamentals of hybrid rocket combustion and propulsion; 2007. https://doi.org/10.2514/4.866876.

[10] Waltrup PJ, White ME, Zarlingo F, Gravlin ES. History of U.S. Navy ramjet, scramjet, and mixed-cycle propulsion development. J Propul Power 2002;18(1):14–27. https://doi.org/10.2514/2.5928.

[11] Foelsche R, Leylegian J, Betti A, et al. Progress on the development of a foreflight atmospheric Scramjet test technique[C]. In: AIAA/CIRA 13th international space planes and hypersonic systems and technologies conference. AIAA; 2005. p. 2005–3297.

[12] Walker S, Rodgers F. The hypersonic collaborative Australia/United States experiment (HyCAUSE)[C]. AIAA/CIRA 13th international space planes and hypersonics systems and technologies conference, AIAA 2005-3254, 2055.

[13] Dolvin D. Hypersonic international flight research and experimentation (Hifire) fundamental science and technology development strategy[C]. In: 15th AIAA international space planes and hypersonic systems and technologies conference. AIAA; 2008. p. 2008–581.

[14] Norris G. HIFire hopes. Aviat Week Space Technol 2011;173(16):41–3.

[15] Kummitha OR, Pandey KM, Gupta R. Numerical analysis of hydrogen fueled scramjet combustor with innovative designs of strut injector. Int J Hydrogen Energy 2020;45(25):13659–71.

[16] Kummitha O R, Pandey K M, Padidam A. Effect of a revolved wedge strut induced mixing enhancement for a hydrogen fueled scramjet combustor. Int J Hydrogen Energy, 2021(4).

[17] Willert C, Jarius M. Planar flow field measurements in atmospheric and pressurized combustion chambers. Exp Fluid 2002;33(6):931–9.

[18] An Bin, Wang Zhenguo, Yang Leichao, Li Xipeng, Zhu Jiajian. Experimental investigation on the impacts of ignition energy and position on ignition processes in supersonic flows by laser induced plasma. Acta Astronaut 2017;137:444–9.

[19] Sun MB, Wang ZG, Liang JH, Geng H. Flame characteristics in a supersonic combustor with hydrogen injection upstream of a cavity flameholder. J Propul Power 2008;24:688e96.

[20] Boyce RR, Mudford NR, McGuire J. OH-PLIF visualisations of radical farming supersonci combsution flows. Shock Waves 2012;22.

[21] Micka D, Driscoll J. Reaction zone imaging in a dual-mode scramjet combustor using CH-PLIF[C]//Aiaa/asme/sae/asee joint propulsion conference & exhibit. 2008.

[22] Jiangbo B, Peng A, et al. Analysis of combustion instability of hydrogen fueled scramjet combustor on high-speed OH-PLIF measurements and dynamic mode decomposition - ScienceDirect. Int J Hydrogen Energy 2020;45(23):13108–18.

[23] Tian Y, Yang S, Le J, et al. Investigation of combustion and flame stabilization modes in a hydrogen fueled scramjet combustor. Int J Hydrogen Energy 2016;41(42):19218–30.

[24] ackson K, Gruber M, Buccellato S. HIFiRE flight 2 project overview and status update 2011[C]. In: 17th AIAA international space planes and hypersonic systems and technologies conference. AIAA; 2011. p. 2011–202.

[25] Jackson K, Gruber M, Buccellato S. HIFiRE flight 2—a program overview[C]. In: 51st AIAA Aerospace sciences meeting. AIAA; 2013. 2013-0695.

[26] Liu Chuping, Long Yongsheng, Bai Hanchen, Zhang Shaowu, Chen Dejiang. Test flow field debugging of scramjet arc heater. Exp Fluid Mech 2005;(4):42–5.

[27] Mitani T, Chinzei N, Kanda T. Reaction- and mixing-controlled combustion in scramjet engines. In: 9th International Space Planes and Hypersonic Systems and Technologies Conference; 1999. https://doi.org/10.2514/6.1999-4871.

[28] Bird GA. A note on combustion driven shock tubes. AGARD Report No 1957;146.

[29] Jiang Zonglin, Li Jinping, Zhao Wei, Liu Yunfeng, Yu Hongru. Long test time detonation-driven shock wave wind tunnel technology. Acta Mech Sin 2012;44(5):824–31.

[30] Jiang Zonglin, Zhao Wei, Lin Zhenbin, Yu Hongru. Research and progress on detonation-driven high enthalpy shock wave wind tunnel and its transient test technology. Adv Mech 2001;(2):312–7.

[31] Li JP, Jiang ZL, Chen H. Numerical study on backward forward double detonation driver for high-enthalpy shock tubes. Chin J Theor Appl Mech 2007;39(3):343–9.

[32] Jiang ZL, Takayama K, Chen YS. Dispersion conditions for non-oscillatory shock capturing schemes and its applications. Comput. Fluid Dyn. J. 1995;4(2):137–50.

[33] Zhang Qifan, Yue Lianjie, Jia Yinan, Zhang Xinyu, Xin Li, Kaohsiung. The influence of real gas effects on the flow of Ma10 inlets. Propulsion Technology 2019;40(5):1042–50.

[34] Brown M, Barone D, Barhorst T, Eklund D, Gruber M, Mathur T, Milligan R. TDLAS-based measurements of temperature, pressure, and velocity in the isolator of an axisymmetric scramjet. In: 46th AIAA/ASME/SAE/ASEE Joint Propulsion Conference & Exhibit; 2010. https://doi.org/10.2514/6.2010-6989.

[35] Yu XL, Li F, Chen LH, Chang XY. A tunable diode-laser absorption spectroscopy (TDLAS) thermometry for combustion diagnostics. In: 15th AIAA International Space Planes and Hypersonic Systems and Technologies Conference; 2008. https://doi.org/10.2514/6.2008-2657.

[36] Jin Y, Zhu Y, Liu K, Xiao F, Yang J. TDLAS-based investigation on thermal parametric shifting caused by air vitiation in hypersonic test. In: AIAA International Space Planes and Hypersonic Systems and Technologies Conference; 2015. https://doi.org/10.2514/6.2015-3689.

[37] Fei Li, Yu Xilong, Gu Hongbin, et al. Simultaneous measurements of multiple flow parameters for scramjet characterization using tunable diode-laser sensors 2011;50(36):6697–707.

[38] Zhou Gongxi, Li Fei, Wang Kuanliang, Lin Xin, Yu Xilong. Research on a quantitative method for three-dimensional computed tomography of chemiluminescence. Appl Opt 2020;59:5310–8.

[39] Wang K, Li F, Zeng H, Yu X. Three-dimensional flame measurements with large field angle. Opt Express 2017;25:21008–18. 570.

[40] Stalker RJ, Morgan RG. The University of Queensland free piston shock tunnel T4 - initial operation and preliminary calibration[C]. Australia: Institution of Engineers; 1988.

[41] Chen Junmou, Xing Chen, Zhixian Bi, et al. Summary of high enthalpy shock wave wind tunnel test technology[J]. Acta Aerodynamics 2018;36(4):543–54.
[42] Fei Li, Yu Xilong, Gu Hongbin, et al. Simultaneous measurements of multiple flow parameters for scramjet characterization using tunable diode-laser sensors. Appl Opt 2011;50(36):6697–707.
[43] Goldenstein CS, Spearrin RM, Jeffries JB, et al. Infrared laser-absorption sensing for combustion gases. Prog Energy Combust Sci 2017;60:132–76.
[44] Li Jinping, Feng Heng, Jiang Zonglin. Gas pollution in shock tunnel induced by the interaction of shock/boundary layer. Acta Mech Sin 2008;(3):289–96.
[45] Berglund M, Fedina E, Fureby C, Tegnér J. Finite rate chemistry large-eddy simulation of self-ignition in supersonic combustion ramjet. AIAA J 2010;48(3):540–50.
[46] Takahashi S, Yamano G, Wakai K, et al. Self-ignition and transition to flame-holding in a rectangular scramjet combustor with a backward step. Proc Combust Inst 2000;28(1):705–12.
[47] Choubey, Gautam, Pandey, et al. Effect of variation of angle of attack on the performance of two-strut scramjet combustor. Int J Hydrogen Energy 2017:11455–70. https://doi.org/10.1016/j.ijhydene.2016.04.048.
[48] Choubey G, Pandey KM. Effect of parametric variation of strut layout and position on the performance of a typical two-strut based scramjet combustor. Int J Hydrogen Energy 2017;42(15):10485–500.
[49] Cai Z, Zhu X, Sun M, et al. Experiments on flame stabilization in a scramjet combustor with a rear-wall-expansion cavity. Int J Hydrogen Energy 2017;42(43):26752–61.
[50] Aravind S, Kumar R. Supersonic combustion of hydrogen using an improved strut injection scheme. Int J Hydrogen Energy 2019;44(12):6257–70.
[51] Ouyang H, Liu W, Sun M. The influence of cavity parameters on the combustion oscillation in a single-side expansion scramjet combustor. Acta Astronaut 2017;137:52–9.
[52] Wang H, Wang Z, Sun M. Experimental study of oscillations in a scramjet combustor with cavity flameholders. Exp Therm Fluid Sci 2013;45:259–63.
[53] Ma F, Li J, Yang V, et al. Thermoacoustic flow instability in a scramjet combustor[C]//Aiaa/asme/sae/asee joint propulsion conference & exhibit. 2013.
[54] Micka DJ. Combustion stabilization, structure, and spreading in a laboratory dual-mode scramjet combustor. The University of Michigan; 2010.
[55] Micka DJ, Driscoll JF. Reaction zon imaging in a dual-mode scramjet combustor using CH-PLIF. AIAA; 2008. p. 5071.
[56] Fei Li, Zhi Li, Gu Hongbin, Yu Xilong, Chen Lihong, Zhang Xinyu. Low Mach number combustion of dual-mode engine Burning oscillation phenomenon. In: The 4th hypersonic science and technology conference. Hainan: Sanya; 2011.
[57] Lumley J. The structure of inhomogeneous turbulent flows [C]. In: Atmospheric turbulence and radio wave propagation. Moscow: Nauka; 1967. p. 166–78.
[58] Zhang Chi, Wang Bo, Zou Pengfei, et al. Concentric swirling stratified flame Statistical analysis of external excitation pulsation characteristics. Journal of Aerodynamics 2017;32(8):1801–8.
[59] Sieber M, Paschereit CO, Oberlaithner K. Advanced identification of coherent structures in swirl-stabilized combustors[C]//ASME turbo expo. 2016. p. 2016.
[60] Michael Stöhr, Sieber M, Yin Z, et al. Experimental study of transient mechanisms of Bi-stable flame shape transitions in A swirl combustor[C]//ASME turbo expo 2017: power for land, sea and air. 2017.
[61] Allery C, Béghein C, Hamdouni A. Applying proper orthogonal decomposition to the computation of particle dispersion in a two-dimensional ventilated cavity. Commun Nonlinear Sci Numer Simulat 2005;10(8):907–20.
[62] Ouyang H, Liu W, Sun M. The influence of cavity parameters on the combustion oscillation in a single-side expansion scramjet combustor. Acta Astronaut 2017;137:52–9.
[63] Lin KC, Jackson K, Behdadnia R, et al. Acoustic characterization of an ethylene-fueled scramjet combustor with a cavity flameholder[C]. In: 43rd AIAA/ASME/SAE/ASEE joint propulsion conference & exhibit; 2010.
[64] Li J, Ma F, Yang V, et al. A comprehensive study of ignition transient in an ethylene-fueled scramjet combustor[C]. In: 43rd AIAA/ASME/SAE/ASEE joint propulsion conference & exhibit; 2007.
[65] Cui Xingda, Sun Mingbo, Wang Hongbo, et al. Study on the influence of injection scheme on low frequency oscillation of cavity flame-stabilized combustor. Propulsion Technology; 2018.
[66] Wickersham AJ, Li X, Ma L. Comparison of Fourier, principal component and wavelet analyses for high speed flame measurements. Comput Phys Commun 2014;185(4):1237–45.
[67] Fleifil M, Annaswamy AM, Ghoneim ZA, Ghoniem AF. Response of a laminar premixed flame to flow oscillations: a kinematic model and thermoacoustic instability results. Combust Flame 1996;106:487–510.